Multiscale insights into mechanical performance of a granite-based geopolymer: Unveiling the micro to macro behavior

Seyed Hasan Hajiabadi [a,*], Mahmoud Khalifeh [a], Reinier van Noort [b]

[a] Department of Energy and Petroleum Engineering, Faculty of Science and Technology, University of Stavanger, 4036, Stavanger, Norway
[b] Department of Reservoir Technology, Institute for Energy Technology, Postbox 40, 2027, Kjeller, Norway

ABSTRACT

Geopolymers (GPs), based on rocks and similar (waste) materials, have shown promising features as alternatives to Ordinary Portland Cement (OPC) in many applications. The properties of these materials can be tailored to a large degree, to meet the requirements of specific applications. This study presents a two-part granite-based GP system developed for wellbore sealant applications in Carbon Capture and Storage (CCS) operations. The system was modified by incorporating different concentrations of a Zn–K-based retarder. The performance of the GP system was then evaluated through consistency analyses, and uniaxial compressive strength (UCS) measurements. Further, the in-situ mechanical attributes of the GP system were assessed through tri-axial experiments at 90 °C and under varying confining pressures. Additionally, the morphology, mineralogy, and chemical composition of the hardened GP system were analyzed using X-ray diffraction (XRD), scanning electronic microscopy with energy dispersive spectroscopy (SEM-EDS), and Fourier transform infrared spectroscopy (FTIR). Consistency analyses revealed that slurries with higher retarder content exhibited improved fluidity but also longer setting times, which could result in fluid invasion and integrity issues. Accordingly, slurries with appropriate setting behavior were identified, striking a balance between rapid strength development and sufficient fluidity for downhole applications. The appropriate flow characteristics of the slurries and the stability of the solidified materials were also verified through rheological assessments, free-fluid tests, and sedimentation analyses. UCS measurements showed a continuous increase in strength for all GP samples, with optimized retarder content yielding the highest late-age mechanical strength. Tri-axial experiments showed that the in-situ Poisson's ratio, compressive strength, and compressive strength to Young's modulus ratio (C/E) of the GP system could be enhanced by 86.79%, 40.26% and 13.05%, respectively, through retarder content optimization. Furthermore, compressive strength and C/E ratios increased with higher confining pressure, while Poisson's ratio remained relatively constant. Moreover, XRD analyses revealed a transition from amorphous to crystalline phases within the GP system, depending on the retarder content, indicating enhanced network connectivity and the formation of new crystalline structures. FTIR analyses supported these observations, demonstrating the formation of new crystals and robust amorphous gels, indicating improved polycondensation and network connectivity in the GP system. Besides, SEM analysis of fractured samples exhibited distinct microstructural characteristics depending on the retarder content, with the optimized retarder content leading to higher crystallinity and more interconnected gel structures. These findings highlight the significance of microscale analysis alongside macroscale assessments when studying GP systems.

1. Introduction

Integrity issues and proper functionality of isolation barriers are among the major concerns over each drilling operation (Khalifeh and Saasen, 2020; Vrålstad et al., 2019). Such loss of barrier integrity might arise from mechanical failure or chemical degradation of isolation materials when they are exposed to physically and/or chemically aggressive downhole conditions of underground reservoirs (Hajiabadi et al., 2023b; Khalifeh et al., 2018b; Kiran et al., 2017). While Ordinary Portland Cement (OPC) is currently the most common cementitious material used for wellbore isolation purposes, its brittle mechanical behavior, and relatively poor chemical resistance (as well as its

environmental footprint) have led researchers to develop alternative materials with more suitable properties. Among the best-known alternative materials are super-sulfated cement, calcium sulfoaluminate/a-luminate cement, pozzolanic-based slurries, bismuth-based metals, unconsolidated materials, thermosetting resins, and geopolymers (GPs) (Kamali et al., 2022a, 2022b; Khalifeh, 2016; Khalifeh et al., 2016a).

GPs are low Ca-content alkali-activated aluminosilicates with long polymeric chains. They can be synthesized through alkali activation of a wide range of reactive aluminosilicate precursors using liquid activators, such as NaOH, KOH, Na_2SiO_3, and K_2SiO_3. The most commonly considered precursors for GP synthesis include fly ash, rice husk ash, metakaolin, red mud, blast furnace slag, glass product wastes, mine tailings, and naturally occurring rocks (Davidovits, 2008, 2013; Duxson et al., 2007; Nadeem et al., 2021; Xiao et al., 2020). Since the introduction of the term GP by Davidovits (Davidovits and Davidovits, 2020), tremendous efforts have been made to explore the application of these materials in construction industry, coating purposes, refractory applications, etc. (Longhi et al., 2019; Rong et al., 2021). Likewise, the notable features of GPs triggered petroleum scientists to investigate the possible application of these materials in well cementing and plugging and abandonment (P&A) operations (Chamssine et al., 2022b; Kamali et al., 2021b).

Recently, there has been a growing focus on rock-based precursors (e.g., aplite, granite, norite) in GP systems due to their favorable mineralogical characteristics, cost-effectiveness, and abundant availability (Eid et al., 2021; Hajiabadi et al., 2023a, 2023b; Khalifeh et al., 2016b, 2017a, 2019). Moreover, as rock-based GPs commonly make use of waste materials, such as mine tailings, which would typically be deposited in landfills, while offsetting traditional binders such as OPC, they can contribute to climate-change mitigation (Davidovits and Davidovits, 2020; Kamali et al., 2022b; Khalifeh et al., 2017b, 2018a).

GPs offer several advantages over OPCs, including reduced chemical shrinkage, enhanced resistance to acid attack and fire, and the ability to immobilize toxic materials (Khalifeh et al., 2015; Tchadjié et al., 2016; Yao et al., 2015; Zhang et al., 2011). Moreover, as evidenced by a large number of researchers, GPs typically have lower permeability and comparable mechanical durability to OPC-based materials (Castillo et al., 2021; Hajiabadi et al., 2023a; Hardjito et al., 2004; Nasvi et al., 2014a, 2014c; Nath et al., 2016; Ramujee and PothaRaju, 2017; Singh and Middendorf, 2020). However, despite these promising features, the field-scale application of GP systems is held back by uncertainties surrounding their mechanical durability under the high-pressure high-temperature (HPHT) conditions encountered in geological reservoirs (Chamssine et al., 2021, 2022b; Chindaprasirt et al., 2007; Nath and Sarker, 2014; Nematollahi and Sanjayan, 2014; Ogienagbon and Khalifeh, 2022; Yaseri et al., 2017).

This paper aims to demonstrate a granite-based GP system developed specifically for application as a wellbore sealant during CCS, using Zn–K based retarders to tailor fluid properties as well as mechanical properties of the hardened material. The retarder-content was optimized to achieve the best mechanical performance while maintaining long enough workability alongside proper rheological features and stability to enable pumping of a slurry to a realistic downhole depth. Next, it presents an investigation into the link between microstructure and mechanical properties of this GP, under relevant in-situ conditions, to gain a better understanding of its performance. This was done through analyzing in-situ GP mechanical properties, mineralogy, morphology, and chemical bonding between silicon and its neighboring elements.

2. Materials and methods

Fig. 1 exhibits a workflow of the analyses performed in this research.

2.1. Materials

A normalized formulation for a low Ca-content GP (less than 10 wt%) was produced by mixing a naturally occurring aluminosilicate rock, as the main precursor, with active quenched Ground Granulated Blast Furnace Slag (GGBFS), and micro-silica. The used rock was a powdered granite (from southwestern Norway), with a particle size in the range of 5–150 μm, which was used in these tests without any further modifications. Granite is one of the most common plutonic rocks in the upper continental crust of Earth. As it mainly consists of quartz, K-feldspars, and biotite, it provides the advantage of high aluminosilicate contents required for GP synthesis (Klein and Philpotts, 2013; Muraleedharan and Nadir, 2021; Nadeem et al., 2021; Nuaklong et al., 2021; Okrusch and Frimmel, 2020; Roper et al., 2016; Tchadjié et al., 2016). However, as granite is relatively slow-reacting due to its crystalline content, an early strength booster is required. A highly reactive GGBFS with high Ca-content (33.74 wt%) was used to enhance the geopolymerization rate and reactivity of the system through the formation of C-A-S-H (calcium aluminosilicate hydrate) gels (Khalifeh et al., 2018c; Nath and Kumar, 2013; Omran et al., 2023; Zhang et al., 2013). The coexistence of (N, K)-A-S-H (sodium/potassium aluminosilicate hydrates) and C-A-S-H gels in GPs results in internal confinement and increased early-age compressive strength of the systems (Hajiabadi et al., 2023b; Kamali et al., 2021a; Khalifeh et al., 2017a, 2017b; Provis and Van Deventer, 2009; Prusty and Pradhan, 2020). Commercial micro-silica, mainly consisting of ultra-fine amorphous SiO_2 spheres, with a density range of 260–380 kg/m^3, was added in small quantities for various purposes, including acting as an efficient reactive micro-filler that decreases the GP's permeability, adjusting the SiO_2/Al_2O_3 ratio, enhancing the formation of nucleation sites required for geopolymerization, and consequently improving the mechanical durability of the system (Alvi et al., 2020; Assi et al., 2018; Khalifeh et al., 2016a, 2016b; Khater, 2013). Limited quantities of micro-silica were used to avoid weakening of the GP structure through excessive self-desiccation and cracking (Hajiabadi et al., 2023b; Khater, 2013). The chemical composition of the normalized solid precursor is shown in Table 1. The development of this granite-based GP is explained in more detail in the work carried out by Khalifeh et al. (2016b).

In this work, a potassium silicate solution with a modulus ratio (SiO_2/K_2O) of 2.14 was used as activating hardener. Deionized water was added to adjust the viscosity and water content of the system, and also to provide a solution medium for chemical admixtures. In addition, potassium nitrate (KNO_3) and zinc nitrate hexahydrate ($Zn(NO_3)_2.6H_2O$), both with a purity of above 99%, were used as retarder.

2.2. Preparation of GP specimens

The samples used in this study were prepared following the procedure described by Kamali et al. (2021b). Table 2 presents the mix
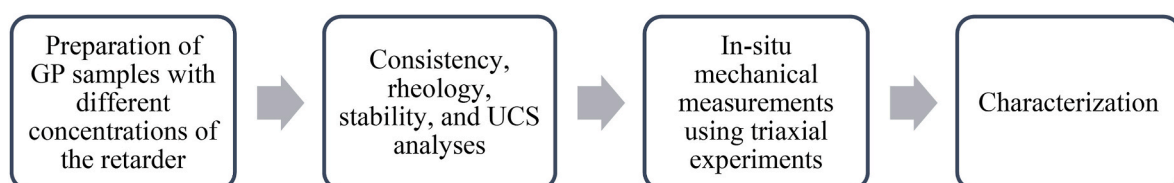

Fig. 1. A workflow of the experimental analyses of this study.

Table 1
Chemical analysis of the solid phase used in the experiments.

Element	SiO_2	Al_2O_3	CaO	Fe_2O_3	K_2O	Na_2O	MgO	TiO_2	MnO	L.O.I
Normalized solid phase	63.1	12.97	9.94	1.49	3.81	2.34	4.54	0.8	0.19	0.82

Table 2
A list of mix design parameters of the slurries employed in the experiments.

Mix design	Solid phase (wt. %)	Liquid phase* (wt. %)	Water/ solid (w/s) ratio	Zn^{2+} in liquid phase (wt. %)	Retarder content in GP (wt. %)
Neat GP	65.3	34.7	0.35	0	0
GP-1	65.2	34.8	0.36	0.54	0.24
GP-2	65	35	0.36	1.06	0.49
GP-3	64.9	35.1	0.36	1.40	0.64
GP-4	64.8	35.2	0.36	1.58	0.73
GP-5	64.7	35.3	0.37	2.09	0.97

design parameters of the GP samples with different concentrations of retarder agents. The K^+/Zn^{2+} ratio in all GP samples was constant at 0.3125 and selected according to the experimental results of several tests previously conducted with different combinations of K^+ and Zn^{2+} (Chamssine et al., 2021, 2022b). In order to ensure homogenization of the solutions, they were allowed to sit for a period of 24 h before being added to the solid phase. Slurry mixing was carried out using a high-speed blender specified in API RP 10B-2 (Rp, 2013).

2.3. Samples conditioning

After the mixing process, the GP slurries prepared for tri-axial experiments underwent conditioning at a predetermined bottomhole circulating temperature (BHCT) of 60 °C. This conditioning was performed using an atmospheric consistometer, gradually raising the temperature from room temperature to the target temperature at a rate of 1 °C/min. Subsequently, the slurries were subjected to stirring at 150 rpm and 60 °C for a duration of 30 min. The purpose of this procedure was to replicate the conditions experienced by the slurries during their downhole placement. Additionally, the conditioning process ensured the uniformity of the slurries and minimized thermal shock to the specimens before undergoing static curing at 90 °C and 13.8 MPa, as the selected bottomhole static temperature (BHST) and bottomhole static pressure (BHSP), respectively (Chamssine et al., 2021; Rp, 2013).

2.4. Consistency analysis

Pumpability of the slurries was studied in the atmospheric consistometer, with the same operational parameters as used for conditioning. Workability is indicative of the time during which the setting material remains in fluid-state prior to the occurrence of gelation. It shows the capability of GP slurry to retain its fluidity throughout circulation and placement in wellbore at target depth (Agista et al., 2022; Kamali et al., 2021b). On the other hand, GP slurry should provide proper setting behavior and highly enough mechanical strength at the desired depth to minimize the rapid invasion of formation fluids, slurry contamination, and resuming well operation (Hamie et al., 2022; Kamali et al., 2021b). According to API RP 10B-2 recommendations, workability is defined as the time required for the consistency of setting materials to reach 100 BCE; however, depending on the operator's criteria one may use 30 to 40BCE as the pumping time. Beyond this time, the elasticity of specimen starts to decrease and slurry becomes risky or even unpumpable (Kamali et al., 2021b; Rp, 2013). Workability depends on a myriad of parameters, mainly including chemical molar ratios, particle size distribution of raw materials, temperature, water content,

and type and concentration of retarders (Khale and Chaudhary, 2007; Nath and Sarker, 2014; Salehi et al., 2019; Yaseri et al., 2017).

2.5. Rheological behavior and stability analyses

Rheological tests were carried out using an atmospheric rotational viscometer specified in API RP 10B-2, operating at the BHCT of 60 °C (Rp, 2013). Viscosity of each slurry was measured under controlled shear rates. To prepare the slurries, they were initially mixed and conditioned using the atmospheric consistometer for a duration of 30 min at the specified BHCT. Each rheological analysis encompassed three distinct phases: pre-shear, ramp-up, and ramp-down. The testing sequence commenced with a pre-shearing stage at a constant shear rate of 100 1/s for a duration of 60 s. This was followed by the ramp-up phase, covering a range from 0.01 to 511 1/s, and subsequently, the ramp-down phase, from 511 1/s back to 0.01 1/s. Furthermore, gel strength was then measured at two instances: 10 s (denoted as Gel strength 10s) and 10 min (denoted as Gel strength 10 m).

In addition, the stability analysis of GP slurries was conducted through two methods: free-fluid test with a static period at ambient temperature, and sedimentation tests. In the free-fluid test, following the recommendations specified in API-RP 10B-2 (Rp, 2013), a graduated cylinder with a capacity ranging from 0 to 250 ml and graduations of 2 ml increments was utilized. After pouring the slurry into the graduated glass cylinder and filling it up to the 250 ml mark, the cylinder was sealed using plastic film wrap to prevent evaporation. After a 2-h undisturbed duration (± 1 min), the volume fraction of free fluid (φ) was calculated based on the volume of free fluid observed on top of the cement slurry.

For sedimentation tests, following one week curing the samples in autoclaves under BHST and BHSP conditions, the demolded specimens were initially designated with markings positioned 20 mm from both the bottom and top. Subsequently, the region between these marks was subdivided into segments of equal length. It is important to note that, throughout the sedimentation tests, concerted efforts were made to maintain the samples submerged in water to prevent any potential drying. Following the precise cutting of the samples at the specified markings, the specific gravity (SG) of each individual segment was assessed using the Archimedes method to evaluate the potential for sedimentation within each GP sample.

2.6. Mechanical strength analyses

During optimization of the GP formulation, UCS measurements were performed to evaluate the efficiency of chemical modification. Once an optimal formulation was developed, its in-situ mechanical strength was assessed through tri-axial experiments under in-situ conditions. Note that all UCS and tri-axial results reported here represent the average values of three samples to minimize the uncertainty of the tests. The samples used for UCS experiments have a diameter of roughly 50 mm and samples prepared for tri-axial experiments have 38 mm in diameter.

2.6.1. Uniaxial compressive strength experiments

An automatic mechanical tester was used for UCS measurements with a loading rate of 71.16 kN/min, in accordance with API TR 10TR7 2017 recommendations (API, 2017). For UCS experiments, the conditioned slurries were transferred to cylindrical plastic molds, and then cured under the BHST and BHSP for 3, 7, and 14 days. The length of plastic molds was greater than or equal to two times of their diameter, as recommended by the API TR 10TR7 2017 for mechanical strength

measurements (API, 2017; Duxson et al., 2005). Before running the tests, the samples ends were cut and ground to guarantee uniform distribution of the applied forces. Then, GP samples were loaded between two parallel plates according to NS-EN 196-1 standard (Astm, 2013; EN, 2005). Note that while the samples were cured in autoclaves at elevated pressure and temperature, the UCS experiments were conducted at ambient conditions.

2.6.2. Tri-axial experiments

To analyze the GP's mechanical performance under in-situ conditions, tri-axial tests were conducted in accordance with the procedures recommended in API TR 10TR7 2017 (API, 2017). Samples for each tri-axial test were conditioned, and then molded in cylindrical rubber sleeves, to be cured at the BHST and BHSP. After one-week curing in autoclave, the autoclaves were slowly depressurized and cooled down to minimize the risk of pressure- or thermal-induced shocks (Rp, 2013). Next, the samples were cut to the desired dimensions using a lathe and the sample ends were ground flat (Ogienagbon and Khalifeh, 2022).

During the tri-axial tests, an extensometer placed around the middle of each specimen provided continuous observation of its radial deformation, while the axial deformation was measured using a linear variable differential transformer (LVDT) connected to the top of the loading piston. After heating to 90 °C, samples were first loaded hydrostatically, ramping up axial and radial stresses simultaneously, at a constant loading rate of 5 MPa/min, up to the target confinement pressure of 13.8 MPa. Subsequently, axial loading was increased with a constant loading rate of 10 MPa/min. Note that these loading rates were selected based on the recommendation provided by API TR 10TR7 2017 (3.5–14 MPa/min) (API, 2017).

2.7. Sample characterization

The chemical bonds between different elements of the GP systems were analyzed using Fourier transform infrared spectroscopy (FTIR) (Agilent Carry 630, US). With a wavelength spectrum ranged between 650 and 4000 cm^{-1}, FTIR experiments characterized the GPs chemical bonds according to infrared light adsorption at various frequencies (Ismail et al., 1997; Smith, 2011). Sample mineral compositions were analyzed using X-ray diffraction (XRD) analysis (Bruker-AXS Micro-diffractometer D8 Advance, with Cu-Kα radiation source, $\lambda = 1.5406$ Å, 40 kV, and 25 mA). During XRD analysis, a 2θ range of 5–70° was applied to record the X-ray patterns. In addition, developing microstructures of the setting materials were studied using a scanning electron microscope (SEM) equipped with a backscattered electron detector (BSD) and energy dispersive spectroscopy (EDS) analyzer (Zeiss Supra 35VP model).

To prepare the samples for these analyses, they were dried at 40 °C overnight, and stored in a vacuum-dryer for one day to eliminate any remaining moisture. Samples were then powdered for XRD and FTIR analyses, while plates were prepared from these samples for SEM-EDS studies. SEM-EDS analyses were conducted after a two-month vacuum treatment following one-week curing at 90 °C and 13.8 MPa. The purpose was to enhance contrast in the microstructure for better image interpretation. The initial one-week period did not yield noticeable differences in SEM images, necessitating the extended waiting time and vacuum treatment for improved sample characterization.

3. Results and discussion

3.1. Consistency analyses

Fig. 2 presents curves of slurry consistency against time, and shows that higher concentration of the Zn–K based retarder leads to longer slurry workability and setting time. The retardation effects arise from the inhibitory mechanism of Zn^{2+} on geopolymerization reactions, primarily due to the precipitation of calcium-zinc phases (Ca(Zn
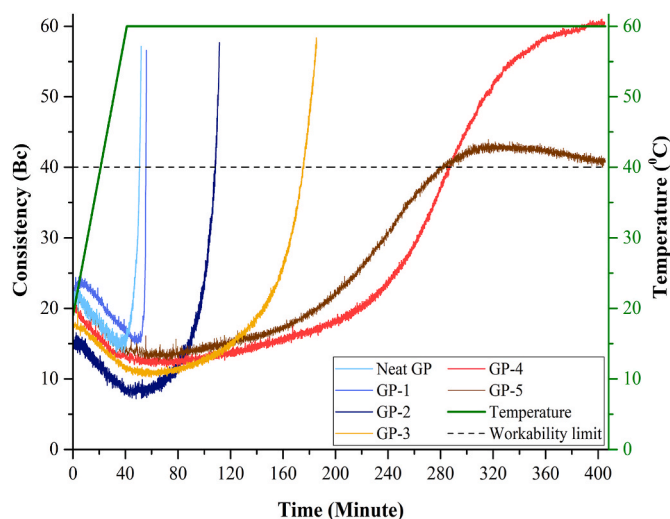

Fig. 2. Atmospheric consistency of GP specimens. The black dashed line indicates the workability limit.

$(OH)_3)_2.2H_2O$. This precipitation leads to a reduction in the number of nucleation sites and a decline in the formation of calcium aluminosilicate hydrates (C-A-S-H), thereby prolonging the condensation process and further impeding the geopolymerization reaction (Chamssine et al., 2022a, 2022b). In addition, the reactions between Zn^{2+} species and the monomeric silica in activator solutions can result in the formation of silicate-zinc complexes (e.g., $[(HO)_3ZnOSiO_2OH]^{4-}$ or $[(HO)_3ZnO(SiO_2)O(SiO_2)OH]^{6-}$), reducing the availability of monomeric silica, thus leading to prolonged setting times (Nedunuri and Muhammad, 2022). Additional experimental data have shown that alkali-activation reactions can be further inhibited through the precipitation of Na/Zn–K containing phases (e.g., (Na/K) (Zn(OH)_3))·nH_2O) (Wang et al., 2020). The tendency of Zn^{2+} towards capturing OH^- and producing zinc hydroxide might also contribute to the poisoning and retardation mechanisms (Chamssine et al., 2022b).

Table 3 shows the workability of the GP slurries, which is the time needed for the slurry consistency to reach 40 BCE (Rp, 2013). GP-4 and GP-5 (containing 0.73 wt% and 0.97 wt% of the retarder, respectively) exhibit the longest workability, which can lead to increased risk of fluid invasion, and negatively impact the material integrity. In contrast, the workability of neat GP (no retarder) and GP-1 (0.24 wt% of retarder) are too short for practical use in zonal isolation. Thus, GP-2 and GP-3, demonstrating appropriate setting behavior for zonal isolation purposes, were selected for further analysis and development. GP-5 was also studied further as a reference, and to provide insight into the impacts of excess retarder content on the mechanical durability of the GP system.

3.2. Rheological behavior and stability analyses

Fig. 3a–c presents the results of flow behavior analysis conducted on GP-2, GP-3, and GP-5 samples following a 30-min conditioning process at BHCT (60 °C). The rheological data clearly exhibit a substantial

Table 3
Workability of GP slurries at 60 °C (selected BHCT) and atmospheric pressure.

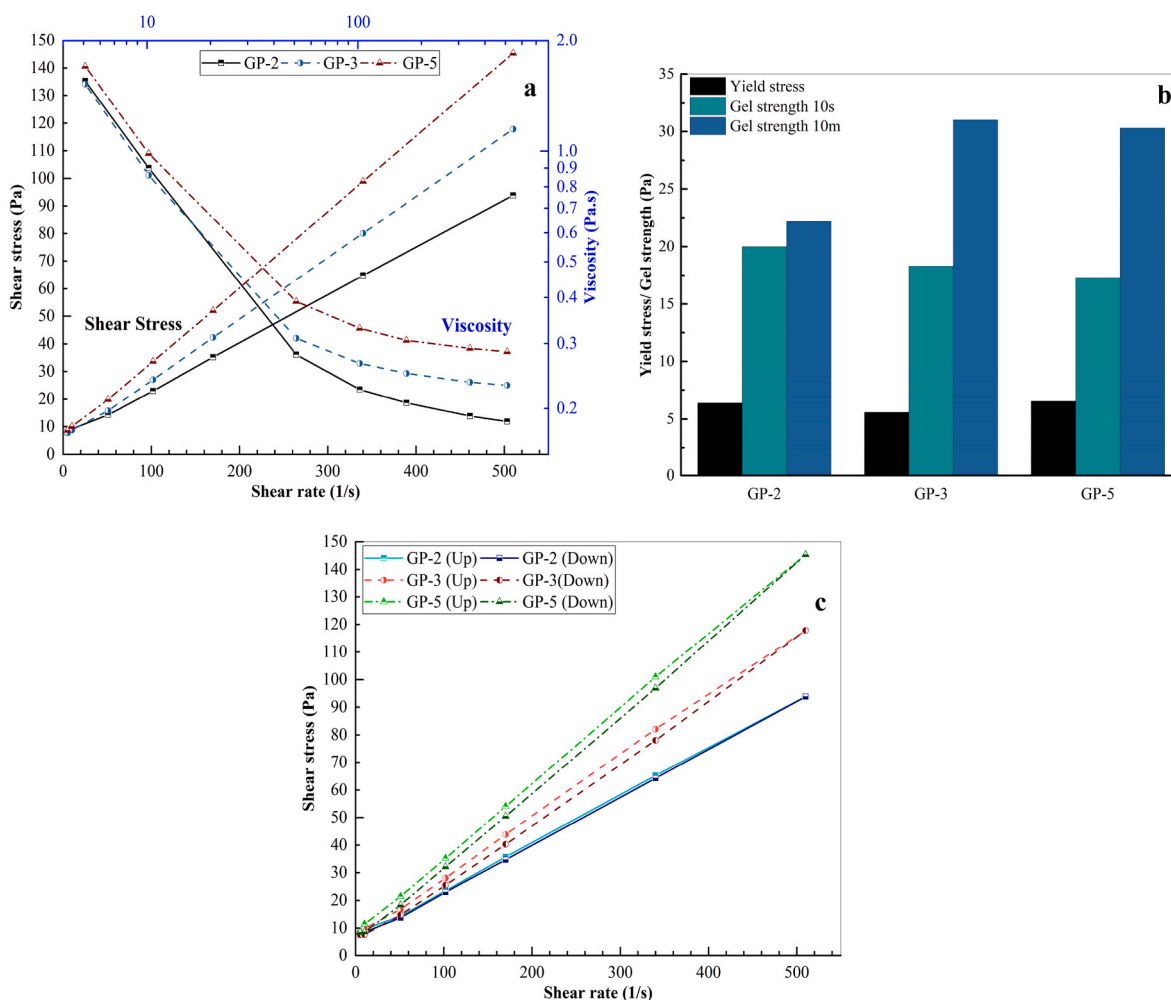| Mix design	Zn^{2+} in liquid phase (wt. %)	Retarder content in GP system (wt. %)	Workability to 40BCE (minutes)
Neat GP	0	0	50.75
GP-1	0.535	0.24	55.60
GP-2	1.062	0.49	108.32
GP-3	1.395	0.64	175.41
GP-4	1.582	0.73	279.3
GP-5	2.094	0.97	282.3

Fig. 3. Representation of rheograms (a), yield stress, gel strength 10s, gel strength 10 m (b), and the ramp-up and ramp-down behavior (c) of the selected GP samples following conditioning at BHCT conditions.

decline in flow resistance with increasing shear rate, indicative of the shear-thinning behavior of the GP slurries (Fig. 3a). This phenomenon can be primarily attributed to the reorientation of GP constituents and the breakdown of the entanglement network within the system as shear rates progressively increase (Darzi et al., 2022; Omran et al., 2022).

The rheological behavior of GP slurries is primarily fitted to the Bingham plastic model. Notably, while no significant difference was observed in the yield stress of the GP slurries, GP-3 and GP-5 exhibit greater gel strengths at both 10 s and 10 min when compared to GP-2. The higher gel strength observed with increased retarder content can be attributed to the Zn–K-based retarder's impact on augmenting the number of nucleation sites and facilitating the precipitation of gel-like structures. In contrast to gels induced by chemical curing, these structures may undergo disintegration when exposed to shearing forces (Khalili et al., 2023). It is crucial to note that GP samples might display pronounced time-dependent rheological behavior. This phenomenon arises from the fact that their flow behavior characteristics can vary significantly based on the specific geopolymerization reactions (dissolution, transportation, polycondensation, etc.) occurring within a defined timeframe.

Moreover, Fig. 3c provides further confirmation of the earlier findings. In the case of GP-2, the ramp-up and ramp-down curves nearly coincide, consistent with the nearly identical gel strengths at 10s and 10 m. Conversely, the widened gap between the ramp-up and ramp-down curves for GP-3 and GP-5 aligns well with the notable difference in gel strengths 10s and 10 m observed in these GP samples, due to the effects

of the Zn–K-based retarder. It is also worth noting that, for all GP samples, the ramp-down curve consistently remains below the ramp-up curves. This observation highlights the thixotropic behavior of the GP systems, which is considered a favorable characteristic for isolation barriers (Khalili et al., 2023).

The results of the API static fluid-loss tests, as presented in Table 4, demonstrate the notably low fluid loss of GP samples within the recommended testing duration. This exceptional fluid loss performance suggests that the water introduced into the mixtures becomes chemically bound during the geopolymerization process, thereby enhancing the structural integrity and durability of the GPs. In practical cementing operations, effective fluid loss control is crucial as excessive infiltration of fluids into the adjacent formations can affect the rheological characteristics and workability of slurries, potentially compromising well barrier integrity. While operators have posed different specifications concerning the acceptable range of fluid loss, values below 50 mL per 30 min are broadly considered advantageous for primary cementing purposes (Kamali et al., 2021b). As a result, the significantly low fluid loss

Table 4
Results of stability analyses of GP slurries performed through free-fluid tests.

Mix design	Measured free fluid volume (mL)	Volume fraction of free fluid (φ) in slurry (%)
GP-2	<1	<0.4
GP-3	<2	<0.8
GP-5	<2	<0.8

observed in the GP systems highlights their promising potential as sustainable isolation barriers in practical operational contexts.

Fig. 4 presents the results of the stability analysis of solidified samples as SG measurements along lengths of sample. While this shows a minor decrease in SG along each GP sample, these changes are notably minimal and insignificant, particularly for GP-3 and GP-5. The somewhat more pronounced sedimentation effect observed in GP-2 likely stems from its higher proportion of unreacted particles that persist due to the shorter dissolution time in GP-2 compared to GP-3 and GP-5 (which had higher retarder contents).

3.3. Uniaxial compressive strength measurements

Fig. 5 shows the results of UCS analysis of GP-2, GP-3, and GP-5 after 3, 7, and 14 days curing at 90 °C and 13.8 MPa. The UCS measurements show continuous strength development and no plateau achieved for all samples (Fig. 5a). Previous studies of these GPs at 100 °C and 50 MPa have shown strength development up to one year (Khalifeh et al., 2017b). Furthermore, while GP-2 showed the fastest development in UCS initially, having the highest UCS after 3 days, GP-3 showed the highest UCS after 7 and 14 days. This shows that in GP-2, high early strengths are caused by high pozzolanic reactions at insufficient retarder content, leading to a more porous structure through very rapid gel formation, that then leads to low final mechanical strength (Bergna and Roberts, 2005).

Fig. 5b presents the development of Young's moduli with curing time. As materials with a lower Young's modulus have higher ductility, it is assumed that they are more efficiently able to resist mechanical stresses encountered downhole, and are, thus, of less susceptibility to failure (Nasvi et al., 2014a, 2016). While the differences in the Young's moduli of the samples tested are relatively minor, it is interesting to note that the Young's moduli of GP-2 and GP-5 continue to increase during curing, while the Young's modulus of GP-3 appears to have plateaued after 7 days. Furthermore, an interesting trend emerges, wherein the Young's Modulus of both GP-2 and GP-3 surpasses that of GP-5, potentially due to differences in gel content in the GP samples, as will be explored below when discussing the micro-scale characterization analyses. Here it should be noted that due to limitations in the accuracy with which axial displacement can be tracked in these UCS tests, the elasticity values reported here should be considered lower bounds, so these results mostly provide qualitative comparisons.
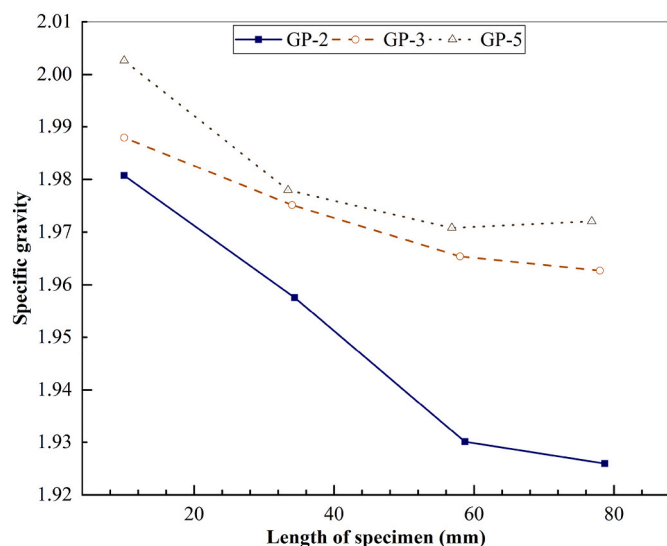
3.4. Tri-axial experiments

3.4.1. In-situ mechanical behavior of the setting materials

Fig. 6 depicts the stress-strain curves of GP-2, GP-3, and GP-5 obtained in the triaxial apparatus under in-situ pressure and temperature. Table 5 provides the compressive strengths, Young's moduli, and Poisson's ratios of the GP samples.

As the results show, after 7 days curing, the excess retarder content of GP-5 (0.97 wt%) compared to optimized formulation GP-3 (0.64 wt%) resulted in a 29% decrease in compressive strength, and a 19% increase in Young's modulus. In GP-2, a lower-than-optimal retarder content (0.49 wt%) led to a 13% reduction in compressive strength and a 12% decrease in Young's modulus. Furthermore, Poisson's ratio was observed to increase with decreasing retarder content. One should note that higher Poisson's ratios are preferred as they lead to reduced destructive hoop stresses, lower magnitude of locally induced stresses in cementitious material, decreased risk of mechanical failure, and improved long-term wellbore integrity (Ogienagbon and Khalifeh, 2022).

Finally, to better understand the impact of formulation amendment on GP performance, compressive strength to Young's modulus (C/E) ratios of the materials were determined, as for zonal isolation purposes, C/E ratios are considered more informative and crucial than the values of the individual parameters (Kamali et al., 2021b; Ogienagbon and Khalifeh, 2022). The highest C/E ratio was observed for GP-3, which thus shows the most favorable mechanical performance of the compositions selected.

3.4.2. Effect of confining pressure on mechanical properties

Comparison of the data reported above for GP-3, shows that confinement pressure influenced the mechanical behavior of this material (see Fig. 7). As the confining pressure increased up to 13.8 MPa, the compressive strength and durability of GP-3 increased (see Fig. 7a). However, confining pressure had only limited effect on the Young's modules, consistent with previously obtained results by Ogienagbon and Khalifeh (2022). Here, it is worth repeating that the relatively low Young's modulus obtained in the UCS test may be due to temperature conditions (ambient temperature in the UCS analyses compared to 90 °C in tri-axial tests) or due to the error in displacement reading on the UCS machine. Poisson's ratios likewise were not affected by confining pressure (see Fig. 7c). This reveals the proper resistance of GP-3 against local stresses induced at different confining pressures and shows the integrity of this cementitious material at presented downhole conditions. Finally, Fig. 7d suggests that the mechanical durability of GP-3 may improve with increasing confining pressure, as C/E reported here increases.

3.4.3. Cohesion and internal friction angle

Analysis of the triaxial measurements obtained on GP-3 based on the Mohr-Coulomb (MC) failure criterion allows for determination of the cohesion strength and internal fiction angle of these samples. This analysis shows that while GP-3 has a high cohesion strength of 6.2 MPa, comparable to that of neat class G cement (Ogienagbon and Khalifeh, 2022), it also has a relatively low angle of friction (3.243°) (see Fig. 8). As GPs typically have low permeabilities (Nasvi et al., 2013, 2014a, 2014b, 2016), this low angle of friction, when compared to similar materials and OPC in (Ogienagbon and Khalifeh, 2022), may have resulted from a build-up of internal pore pressures during the rapid axial loading applied in accordance with API TR 10TR7 2017 (Das and Sivakugan, 2018; Ekawita et al., 2015; Hansbo, 1994). Similar influence of loading rates on the MC-criterion have been reported for other materials, including sandstones (Si et al., 2019).

3.5. Compositional and microstructural characterization

To gain deeper insights on how retarder content impacts the GP mechanical properties through affecting its composition and
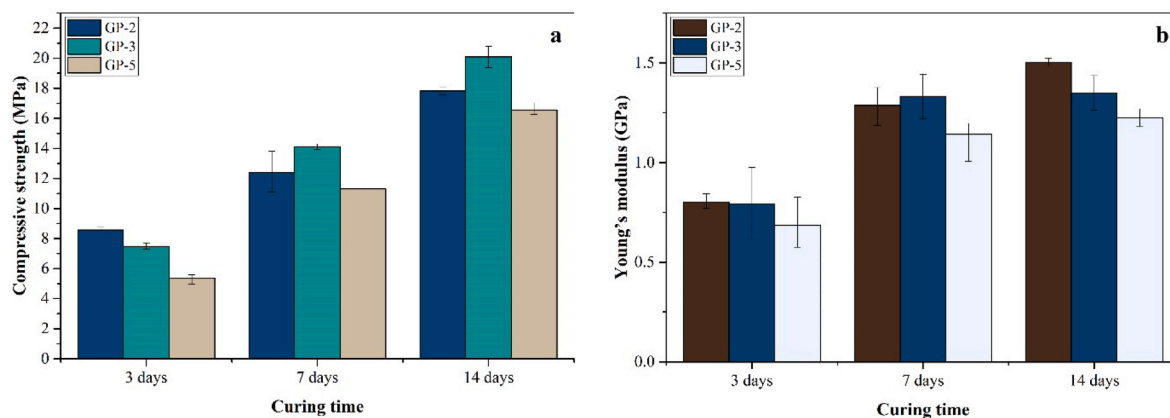

Fig. 4. Results of stability analyses of solidified GP samples performed through sedimentation tests.

Fig. 5. Uniaxial compressive strengths (a) and Young's moduli (b) of GP-2, GP-3, and GP-5 at different curing times.
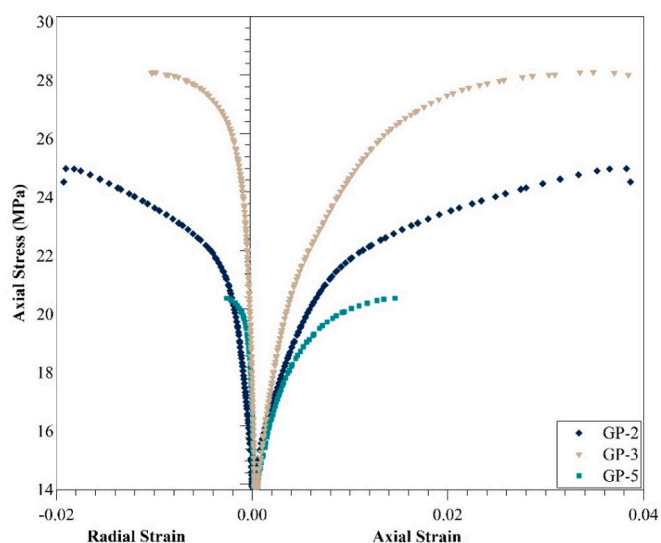

Fig. 6. Stress-strain curves of GP-2, GP-3, and GP-5 samples at 90 °C and 13.8 MPa.

Table 5
An illustration of the in-situ mechanical properties of GP-2, GP-3 and GP-5 samples according to tri-axial analyses.

Mix design	Compressive strength (MPa)	Young's modulus (GPa)	Poisson's ratio	C/E ratio (MPa/GPa)
GP-2	24.80	1.573	0.259	15.76
GP-3	28.56	1.796	0.160	16.15
GP-5	20.36	1.456	0.086	14.28

microstructure, a series of material characterization analyses was conducted using XRD, SEM with EDS, and FTIR.

3.5.1. XRD analysis

Fig. 9 presents the results of XRD analyses performed on GP-2, GP-3, and GP-5 samples after a one-week curing period at 90 °C and 13.8 MPa, as well as on the solid precursor mixture (i.e., comprising granite, GGBFS and micro-silica). The humps in the XRD pattern of the species are an indication of the amorphous content of each material. Estimations of the crystalline fraction from these spectra (see Table 6) indicate similar crystalline contents for GP-2 and GP-3, (72–74%), and a significantly lower crystalline content for GP-5 (67%). In GPs, an increase in crystalline content during curing, due to the formation of new

crystalline phases, is typically associated with higher network connectivity (Abdollahnejad et al., 2019; Fernández-Jiménez and Palomo, 2009; Yong-Sing et al., 2022). The results presented in this study demonstrate a correlation between higher crystalline content in the GP and increased mechanical strength and Young's modulus. These findings align with previous reports from other researchers, where even minor increases in GP crystalline content have shown significant enhancements in their mechanical performance (Mani and Pradhan, 2020; Somna et al., 2011).

In addition, while all GP samples exhibited similar mineral distributions (see Figs. 9 and 10), the XRD spectra measured on GP-5 had weaker peaks for all identified minerals (quartz, albite, microcline, chlorite, and biotite, and amphibole), and about 5–6% higher amorphous content compared to GP-2 and GP-3. This difference in crystalline content is primarily attributed to the prolonged duration of the dissolution stage that occurs when an excessive amount of retarder is present, resulting in a significant transformation of the GP precursor's mineral composition into an amorphous state. Furthermore, as highlighted in Section 3.1, the excessive concentration of Zn–K based retarders reduces the number of available nucleation sites, consequently leading to incomplete polycondensation or polymerization steps (as illustrated in Fig. 2). Hence, the complete recrystallization of the newly formed and/ or pre-existing amorphous contents is impeded, resulting in lower compressive strength and Young's modulus.

When comparing the crystalline contents of GP-2 and GP-3, GP-2 contain somewhat higher relative quantities of biotite, chlorite, and amphibole, and lower relative quantities of quartz and feldspars (albite and microcline). A possible cause of these differences is the extended workability of GP-3. This provided more time for the consumption of the slower-dissolving unstable minerals (e.g., micas, amphiboles), and for the condensation and polymerization processes that lead to the formation of more stable minerals such as quartz and feldspars (Kumar et al., 2017; Lutgens et al., 2014; Marshak, 2004). In this manner, the optimized workability of GP-3 contributed to this GP's higher compressive strength. Indeed, these observations align research conducted by Mani and Pradhan (2020) and highlight the increased intensity of the albite peak may be indicative of a higher degree of polymerization, and the formation of N(K)-A-S-H gels that contribute to compressive strength.

3.5.2. SEM-BSD and EDS analysis

The SEM analysis of fractured samples (GP-2, GP-3, and GP-5) after a two-month vacuum treatment following one-week curing at 90 °C and 13.8 MPa are presented in Figs. 11–13. Corresponding EDS analysis results are also presented in Table 7.

SEM-BSD/EDS analysis of GP-2 (Fig. 11) revealed the presence of relatively larger grains, measuring up to 50 μm, embedded within a fine-grained matrix. The matrix exhibits a relatively homogeneous
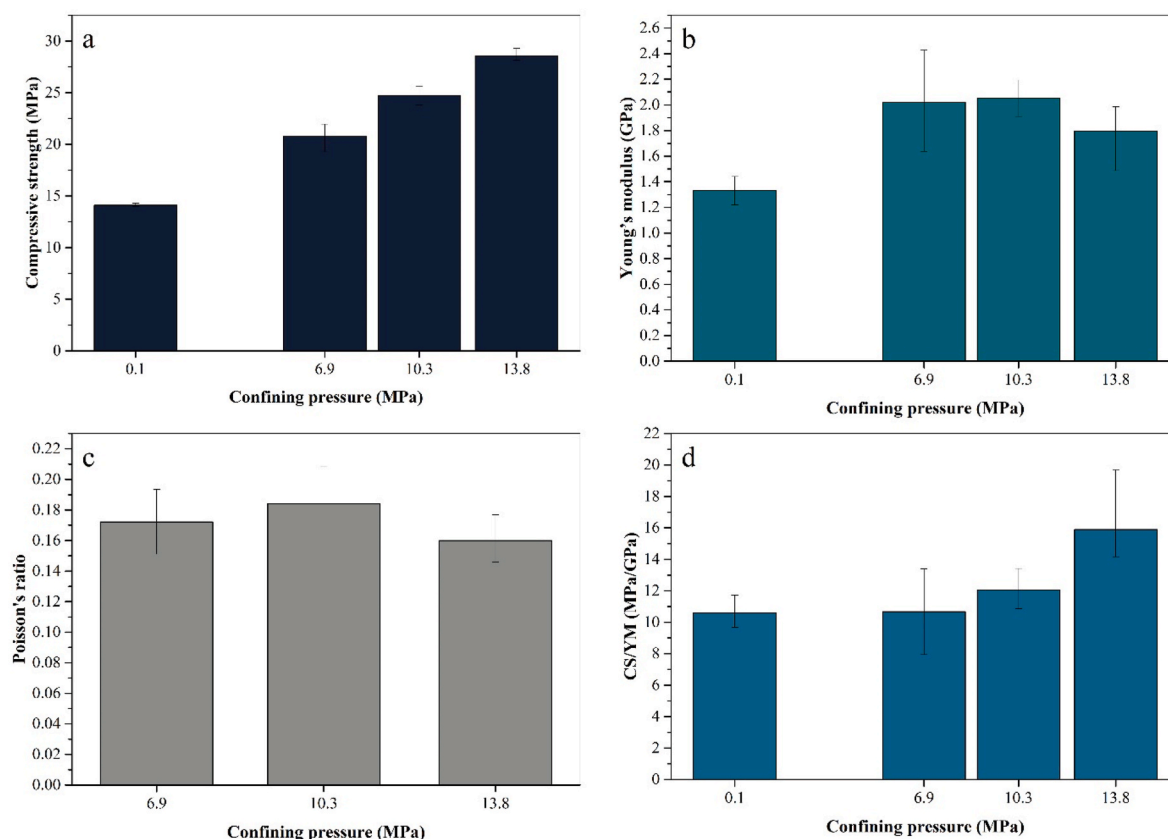
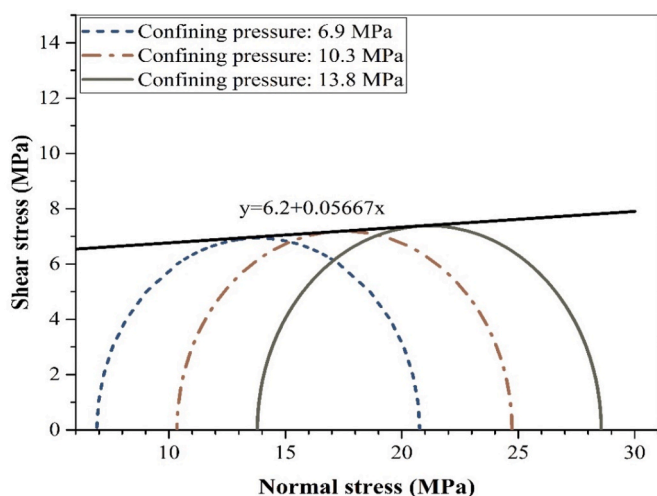**Fig. 7.** Mechanical properties of GP-3 at different confining pressures.

Fig. 8. The shear strength envelope of GP-3 at different confining pressures (6.9, 10.3, and 13.8 MPa).

composition, yet it displays numerous fine cracks, which can be attributed to the drying shrinkage of the GP system occurred during sample preparation in vacuum chamber. Upon closer examination (see Fig. 11, righthand side), it becomes evident that the grains are loosely embedded within the matrix, displaying a low degree of bonding between the grains and the surrounding matrix. In fact, these findings exhibit a low degree of recrystallization, accompanied by the presence of unreacted particles surrounded by amorphous K-A-S-H, C-A-S-H, and Mg-A-S-H (magnesium aluminosilicate hydrate) gels. The restricted workability of this GP sample led to the partial dissolution of less stable minerals (e.

g., chlorite and biotite), while minerals with higher stability, like quartz, remained mostly unaffected by the dissolution processes (referring to Bowen's reaction series) (Shah et al., 2020; Yousefi Oderji et al., 2019). Note that the drying shrinkage should not be a concern as humidity is present in downhole.

In contrast, SEM-BSD/EDS analysis of GP-3 (Fig. 12) demonstrated a reduced presence of unreacted particles and a higher degree of crystallinity, attributed to the recrystallization of amorphous constituents and the formation of new silicate minerals, as also supported by the XRD analyses presented above. EDS analysis also shows that newly formed minerals are supported by an amorphous matrix of K-A-S-H, C-A-S-H, and Mg-A-S-H gel structures. These gel structures not only interconnected the newly formed minerals but also occupied the pore space within the GP network, thereby augmenting the material's strength while ensuring its ductility.

Conversely, the microstructure of GP-5 displayed an inhomogeneous nature with loosely structured particles of varying sizes. Fig. 13 emphasized the significant presence of unreacted particles, including quartz, biotite, microcline, and albite, embedded within an amorphous matrix of K-A-S-H, C-A-S-H, and Mg-A-S-H gels. As previously discussed, the presence of these gels contributes to the system's ductility and mechanical strength; however, an excessive amount of these materials indicates a loose structure and reduced mechanical performance of the GP system. These observations which are aligned with the XRD results can be attributed to prolonged dissolution time and reduced polycondensation/recrystallization processes, primarily influenced by the excessive poisoning impacts of the Zn–K-based retarder.

3.5.3. FTIR analysis

Fig. 14 shows the FTIR analysis results of the GP matrices after one-week curing under elevated pressure and temperature. The intense, wide absorption peaks observed at 965-968 cm^{-1} correspond to the
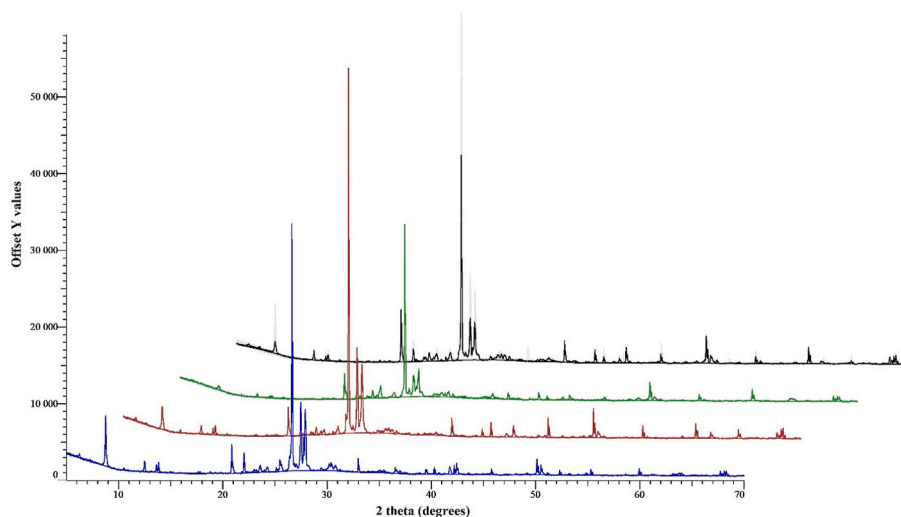
Fig. 9. Waterfall representation of XRD patterns of GP-2 (blue), GP-3 (red), GP-5 (green), and the corresponding precursors (black). The pale grey line visually shows the overlapping XRD patterns, facilitating a comparative analysis of the obtained results.

Table 6
The crystalline and amorphous content of the GP samples, precursors, and total solid phase in the system.

Sample	Crystallinity (wt.%)
GP-2	72.4
GP-3	73.6
GP-5	67.4
Precursors	75.5
Total solid phase in the system[a]	64.2

[a] Determined by considering the combined solid content of the precursors and the hardener. The solid content of the hardener was completely amorphous.

asymmetric stretching vibrations of Si–O–T (T = Si, Al, K). Additional peaks observed at 715-717 cm^{-1} correspond to the symmetrical stretching vibrations of Si–O–Si and Si–O–Al bonds. The stretching vibration of hydroxyl groups (Si–O–H bonds) is observed at 3345-3350 cm^{-1}. Note that the bending vibrations of hydroxyl groups (H–O–H groups) at 1636-1638 cm^{-1} are from water absorbed on the surface or imprisoned in the cavities of GPs (Vafaei and Allahverdi, 2017; Xue et al., 2018; Yaseri et al., 2017).

The wavenumber of Si–O–T asymmetric stretching peak in GP-3 (i.e., 968 cm^{-1}) is higher than that of GP-2 (i.e., 967 cm^{-1}) and GP-5 (i.e., 965 cm^{-1}). The higher wavenumber and lower intensity of the main band in GP-3 denote the formation of new crystals and the presence of robust amorphous N(K)-A-S-H and C-A-S-H gels. These observations suggest a notable degree of polycondensation, and the promotion of network connectivity within the GP matrix (Fang and Zhang, 2020; Pacheco-Torgal et al., 2014; Xue et al., 2018; Yaseri et al., 2017). The reduced intensity of –OH bands is also indicative of growing degree of polycondensation and is characteristic of the maturation of GPs. The more intense –OH bands, especially in GP-5 samples, is due to its higher water content and can be correlated to the diminished mechanical strength of the specimens (Pacheco-Torgal et al., 2014; Yaseri et al., 2017). It should be noted that the bands between 1300 and 1500 cm^{-1} show the stretching vibration of O–C–O bonds, the adsorption characteristics of carbonate groups, and the presence of calcium/sodium carbonates resulting from carbonation of GP samples (Finocchiaro et al., 2020; Pacheco-Torgal et al., 2014; Vansant et al., 1995; Xue et al., 2018). Note that simultaneous preparation of all GP samples ensured result validity and minimized drying-related errors, particularly regarding the interpretation of –OH bands.

4. Integrating the behavior of GPs: bridging the micro and macro perspectives

To better understand how microstructural and compositional properties of the studied GP system may impact its mechanical behavior, the various microscale observations made on GP-2, GP-3 and GP-5, and the mechanical properties of these samples will be compared and correlated in this section. When considering GP-3, both XRD showed this sample to have the highest crystalline content, which was supported by SEM observations showing well-formed crystals embedded in a dense gel matrix surrounding the precursor grains. The relative maturity, and high interconnectivity of this gel matrix was further indicated by FTIR analysis. In contrast, SEM on GP-5 showed an inhomogeneous microstructure of unreacted grains loosely embedded in a dense gel matrix, with grain-gel bonding. The lower maturity of this structure, and relatively low crystalline content of the matrix were confirmed through FTIR and XRD. Comparing these microstructural and compositional observations to the measured macroscale differences in mechanical properties shows how crystallinity, microstructure, and chemical bonding within a GP correlate to its performance. GP-3, characterized by optimized workability and improved microstructural properties such as higher crystalline content and interconnected gel structures, demonstrates higher compressive strength and Young's modulus. On the other hand, the inhomogeneous microstructure and excessive retarder content in GP-5 result in its inferior mechanical performance in the macro-scale tests. The optimized reaction rates in GP-3 may have resulted in strong bonding between dissolving precursor grains, and precipitating product gel and crystals, leading to improved mechanical stability, whereas the inhibited dissolution/polycondensation in GP-5 resulted in a microstructure without such bonding between different phases, and thus lower mechanical stability. These findings highlight the critical role of efficient workability in the development of superior mechanical properties, achieved through the optimization of dissolution and polycondensation/recrystallization duration.

This example thus shows how the integration of micro-scale analyses and the correlations between these micro-scale analyses and the macro-scale tests can be used to better understand a specific GP's properties, and how these may develop over time, and how such improved understanding can facilitate GP-optimization for specific applications, contributing to the advancement of GP technology.
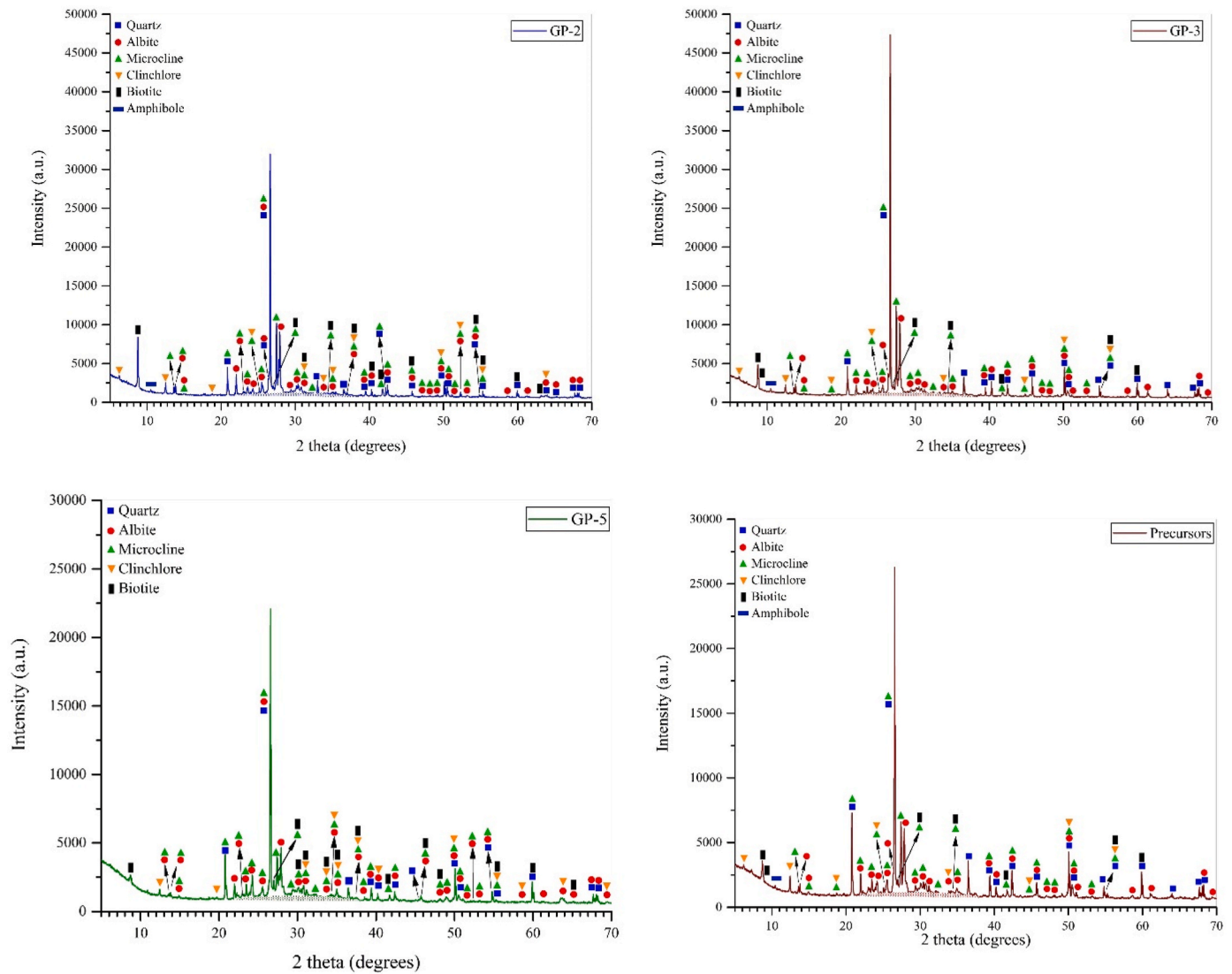
Fig. 10. XRD analysis of GP-2, GP-3, GP-5, following one-week curing at 90 °C and 13.8 MPa, alongside the precursors.
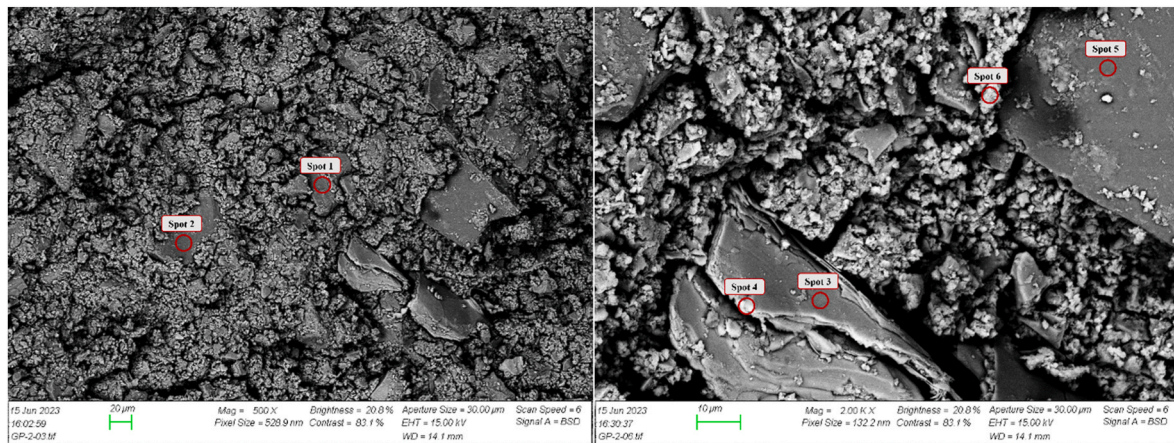

Fig. 11. SEM-BSD images of GP-2 after a two-month vacuum treatment following one-week curing at 90 °C and 13.8 MPa.

5. Conclusions

In this work, the performance of a rock-based geopolymer (GP) system, modified with different concentrations of a Zn–K-based retarder,

was evaluated under pressure-temperature conditions representative of those encountered by a wellbore sealant, with the aim of understanding how the retarder impacted microstructural and compositional properties of the GP that in turn affect its mechanical properties. Atmospheric
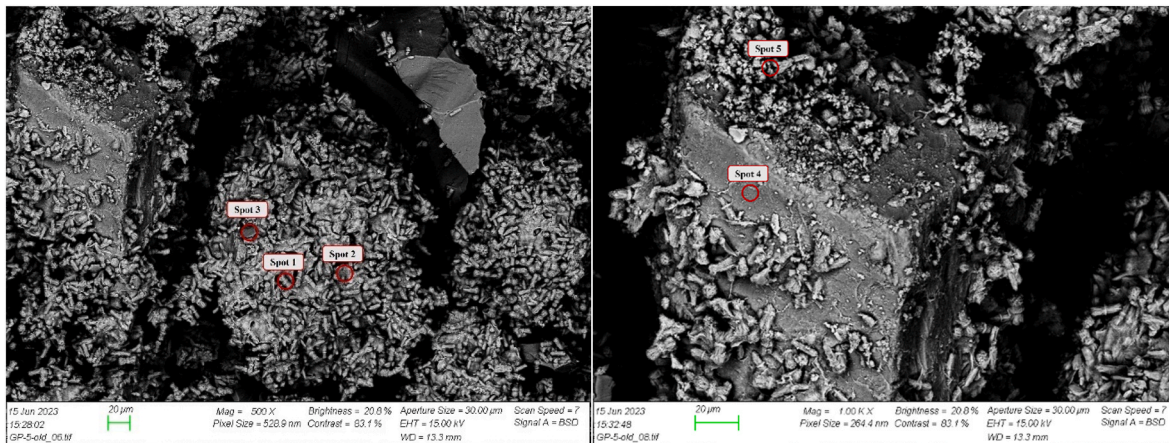
Fig. 12. SEM-BSD images of GP-3 after a two-month vacuum treatment following one-week curing at 90 °C and 13.8 MPa.
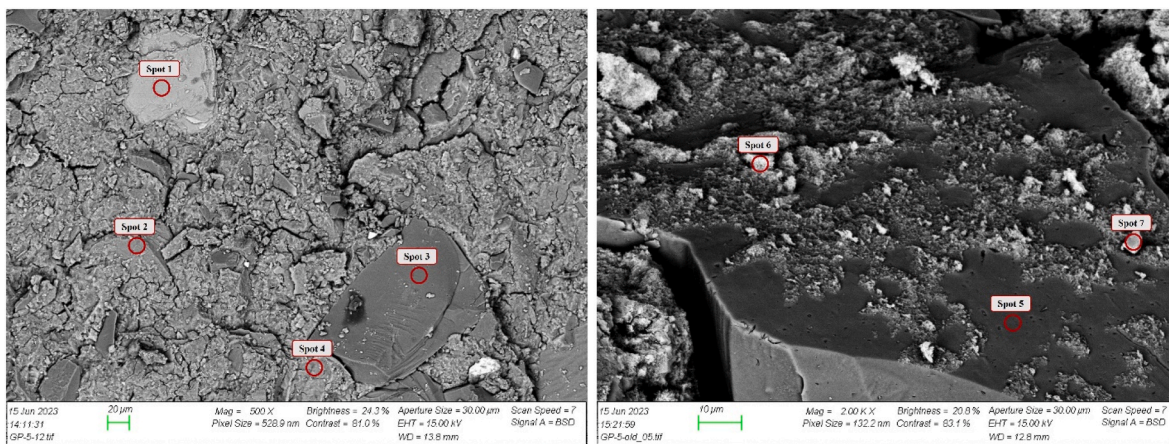

Fig. 13. SEM- BSD images of GP-5 after a two-month vacuum treatment following one-week curing at 90 °C and 13.8 MPa.

Table 7
The results of EDS analysis of GP samples (atomic %) after a two-month vacuum treatment following one-week curing at 90 °C and 13.8 MPa.

Sample	Spot No.	O	Si	Al	Mg	Fe	K	Ca	C	Ti	Cu	Composition
GP-2	Spot 1	65.14	26.47	0.65	0.55	–	0.68	–	–	–	5.51	Quartz
	Spot 2	59.14	31.76	0.85	0.43	–	1.48	0.82	–	–	5.52	Quartz
	Spot 3	57.34	13.06	6.57	4.88	4.83	4.06	–	–	0.80	20.80	Chlorite
	Spot 4	34.41	20.93	4.09	1.24	4.49	12.76	5.81	–	1.21	15.06	K-A-S-H, C-A-S-H, Mg-A-S-H
	Spot 5	51.04	40.07	–	–	–	–	–	–	–	8.88	Quartz
	Spot 6	47.65	22.91	3.57	0.64	–	6.96	2.87	–	–	15.39	K-A-S-H, C-A-S-H, Mg-A-S-H
GP-3	Spot 1	49.24	19.11	6.89	0.64	–	8.34	1.60	–	–	14.18	Zeolites
	Spot 2	53.87	19.56	3.43	0.58	–	10.63	5.08	–	–	6.86	K-A-S-H, C-A-S-H, Mg-A-S-H
	Spot 3	64.66	30.52	–	–	–	–	–	–	–	4.82	Quartz
	Spot 4	62.14	19.45	7.35	–	–	5.60	–	–	–	5.46	Feldspar
	Spot 5	56.05	19.80	4.83	1.54	1.13	6.75	3.36	2.28	0.13	4.13	K-A-S-H, C-A-S-H, Mg-A-S-H
GP-5	Spot 1	45.28	15.45	6.97	2.70	12.72	6.09	–	–	0.69	10.09	Biotite
	Spot 2	51.53	24.38	8.13	–	–	8.27	–	–	–	7.69	Microcline
	Spot 3	62.31	32.48	–	–	–	–	–	–	–	5.21	Quartz
	Spot 4	41.45	22.91	3.60	0.82	0.27	11.15	7.69	–	0.16	11.96	K-A-S-H, C-A-S-H, Mg-A-S-H
	Spot 5	55.51	35.86	0.42	0.07	–	–	–	–	–	8.14	Quartz
	Spot 6	58.96	21.15	1.90	0.99	–	3.55	2.16	0.01	–	11.29	K-A-S-H, C-A-S-H, Mg-A-S-H
	Spot 7	64.80	29.46	–	–	–	–	–	–	–	5.74	Quartz

consistency analyses were conducted at 60 °C, uniaxial testing was performed at ambient temperature, and curing and tri-axial testing were conducted at 90 °C and 13.8 MPa confining pressure. Microscale analyses were also performed using X-ray diffraction (XRD), scanning electron microscopic (SEM) analysis with energy dispersive spectroscopy (EDS), and Fourier transform infrared spectroscopy (FTIR). Key

findings of this study are as follows:

- Consistency analysis (60 °C, atmospheric pressure) confirmed that slurries with higher concentrations of the retarder exhibited better fluidity, as well as longer setting times. Based on this, two slurries demonstrating appropriate setting behavior (GP-2 with 0.48 wt%
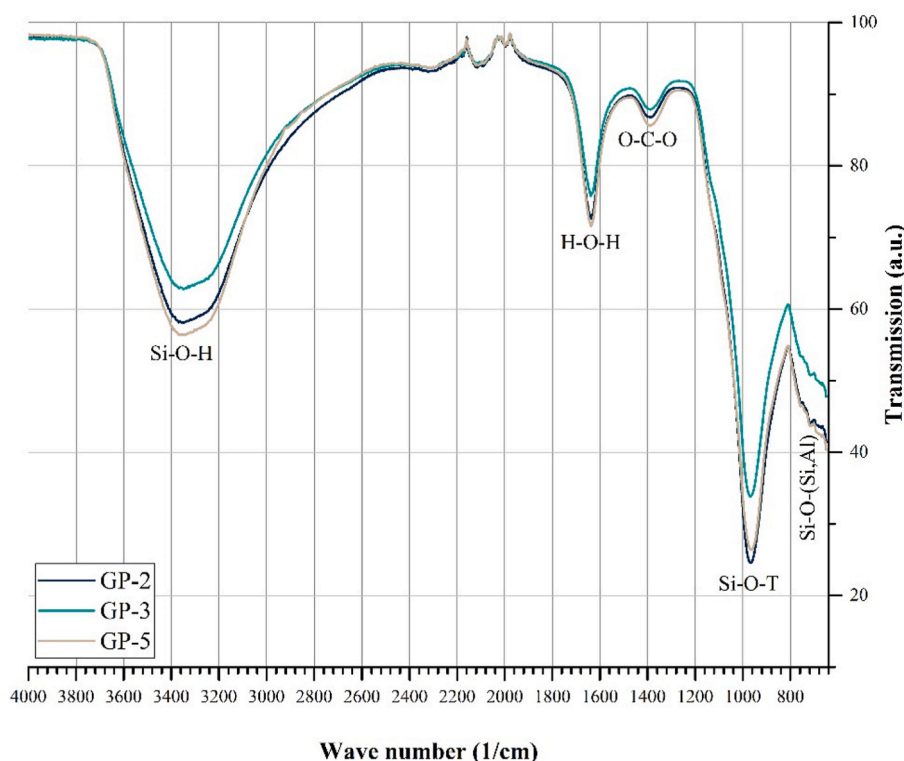
Fig. 14. Fourier Transform Infrared Spectroscopy (FTIR) spectrum of GPs 2, 3, and 5 after one-week curing at 90 °C and 13.8 MPa.

and GP-3 with 0.64 wt% retarder) were selected for further analysis. A third composition with excessive retarder content (GP-5 with 0.97 wt% retarder) was included for reference purposes.

- The UCS (measured at room temperature and atmospheric pressure) increased continuously for all GP samples without reaching a plateau during 14 days of curing. While GP-2 exhibited the highest compressive strength at 3 days, GP-3 achieved higher compressive strengths at 7 and 14 days. The Young's modulus did not show significant dependence on retarder content. Tri-axial testing at 7 days (90 °C and 13.8 MPa confining pressure) showed that, compared to GP-5, GP-3 had higher compressive strength (40%), compressive strength to Young's modulus (C/E) ratio (13%), and Poisson's ratio (87%). Furthermore, the failure envelope of GP-3 showed high cohesion strength, but an extremely low friction angle. This low friction angle was likely the result of pore fluid pressurization due to the relatively high loading rates and very low permeability of GP systems. Future triaxial testing on GPs (and similar low-permeability sealant samples) should be carried out at lower loading rates to reduce the impact of pore fluid pressurization.
- Microstructural analysis on fractured surfaces using SEM with EDS, supported by XRD analysis of crushed samples and FTIR analysis, showed a distinct impact of retarder content. In GP-2, low retarder content resulted in limited recrystallization as shown by the presence of unreacted particles surrounded by amorphous gels, In GP-5, excessive retarder content inhibited nucleation, resulting in a porous and inhomogeneous microstructure, with unreacted particles embedded within highly amorphous gels. In GP-3, the optimized retarder content yielded higher crystallinity as amorphous constituents recrystallized during curing, forming mostly silicate minerals. This higher degree of crystallinity, presence of interconnected gel structures, and formation of stable minerals contributed to its improved strength and ductility.

The findings of this research highlight how incorporating microscale analysis alongside macroscale assessments when studying GP systems

can lead to enhanced understanding and optimization of GP materials for specific applications, thus advancing GP technology. This is of high importance, as one of the key limitations to the application of GPs as wellbore sealants, currently, is their pumpability, the extension of which requires further consideration. To achieve this, further research should consider the impacts of various retarders on both macrostructural and microstructural properties. The variations in experimental conditions and initial materials in the literature represent additional limitations that hinder a meaningful and scientific comparison of the properties of GP systems. Furthermore, the findings also indicate that the current standardized protocols for tri-axial testing of sealants, developed for more permeable OPC-based sealants, should be reevaluated when assessing materials with lower permeabilities, including OPC-based materials with very low permeability and GPs.

Declaration of competing interest

The authors declare that they have no known competing financial interests or personal relationships that could have appeared to influence the work reported in this paper.

Data availability

Data will be made available on request.

(FTIR) analyses.

References

Abdollahnejad, Z., Dalvand, A., Mastali, M., Luukkonen, T., Illikainen, M., 2019. Effects of waste ground glass and lime on the crystallinity and strength of geopolymers. Mag. Concr. Res. 71 (23), 1218–1231.

Agista, M.N., Khalifeh, M., Saasen, A., 2022. In-depth rheological evaluation of gas tight cement for shallow gas application. In: SPE Asia Pacific Oil & Gas Conference and Exhibition. OnePetro.

Alvi, M.A.A., Khalifeh, M., Agonafir, M.B., 2020. Effect of nanoparticles on properties of geopolymers designed for well cementing applications. J. Petrol. Sci. Eng. 191, 107128.

API, R., 2017. API TR 10TR7. Mechanical Behavior of Cement.

Assi, L.N., Deaver, E.E., Ziehl, P., 2018. Using sucrose for improvement of initial and final setting times of silica fume-based activating solution of fly ash geopolymer concrete. Construct. Build. Mater. 191, 47–55.

Astm, C., 2013. 109. Standard Test Method for Compressive Strength of Hydraulic Cement Mortars (Using 2in. Or [50-mm] Cube Specimens)'. Annual Book of ASTM Standards, USA.

Bergna, H.E., Roberts, W.O., 2005. Colloidal Silica: Fundamentals and Applications. CRC Press.

Castillo, H., et al., 2021. Factors affecting the compressive strength of geopolymers: a review. Minerals 11 (12), 1317.

Chamssine, F., Gargari, P., Khalifeh, M., 2022a. Impact of admixtures on pumpability and short-term mechanical properties of rock-based geopolymer designed for zonal isolation and well abandonment. In: Offshore Technology Conference. OnePetro.

Chamssine, F., Khalifeh, M., Eid, E., Minde, M.W., Saasen, A., 2021. Effects of temperature and chemical admixtures on the properties of rock-based geopolymers designed for zonal isolation and well abandonment. In: International Conference on Offshore Mechanics and Arctic Engineering. American Society of Mechanical Engineers, V010T11A031.

Chamssine, F., Khalifeh, M., Saasen, A., 2022b. Effect of Zn2+ and K+ as retarding agents on rock-based geopolymers for downhole cementing operations. J. Energy Resour. Technol. 144 (5), 053002.

Chindaprasirt, P., Chareerat, T., Sirivivatnanon, V., 2007. Workability and strength of coarse high calcium fly ash geopolymer. Cement Concr. Compos. 29 (3), 224–229.

Darzi, H.H., et al., 2022. Carbon-based nanocomposites: distinguishing between deep-bed filtration and external filter cake by coupling core-scale mud-flow tests with computed tomography imaging. J. Nat. Gas Sci. Eng. 105, 104707.

Das, B.M., Sivakugan, N., 2018. Principles of Foundation Engineering. Cengage learning.

Davidovits, J., 2008. Geopolymer Chemistry and Applications. Geopolymer Institute.

Davidovits, J., 2013. Geopolymer Cement. A Review, vol. 21. Geopolymer Institute, pp. 1–11. Technical papers.

Davidovits, J., Davidovits, R., 2020. Ferro-Sialate Geopolymers (-Fe-O-Si-O-Al-O-). Geopolymer Institute Library.

Duxson, P., et al., 2007. Geopolymer technology: the current state of the art. J. Mater. Sci. 42 (9), 2917–2933.

Duxson, P., et al., 2005. Understanding the relationship between geopolymer composition, microstructure and mechanical properties. Colloids Surf. A Physicochem. Eng. Asp. 269 (1–3), 47–58.

Eid, E., Tranggono, H., Khalifeh, M., Salehi, S., Saasen, A., 2021. Impact of drilling fluid contamination on performance of rock-based geopolymers. SPE J. 1–8.

Ekawita, R., Nawir, H., Khairurrijal, K., 2015. A Simple Unconsolidated Undrained Triaxial Compression Test Emulator, Applied Mechanics and Materials. Trans Tech Publ, pp. 104–107.

EN, T., 2005. 196-1. Methods of Testing Cement–Part 1: Determination of Strength. European Committee for standardization, p. 26.

Fang, G., Zhang, M., 2020. Multiscale micromechanical analysis of alkali-activated fly ash-slag paste. Cement Concr. Res. 135, 106141.

Fernández-Jiménez, A., Palomo, A., 2009. 6 - nanostructure/microstructure of fly ash geopolymers. In: Provis, J.L., van Deventer, J.S.J. (Eds.), Geopolymers. Woodhead Publishing, pp. 89–117.

Finocchiaro, C., et al., 2020. FT-IR study of early stages of alkali activated materials based on pyroclastic deposits (Mt. Etna, Sicily, Italy) using two different alkaline solutions. Construct. Build. Mater. 262, 120095.

Hajiabadi, S., Khalifeh, M., Van Noort, R., Moreira, P.S.S., 2023a. Effect of magnesium-bearing additives on the properties of a granite-based geopolymer sealant for CCS. In: 84th EAGE Annual Conference & Exhibition. European Association of Geoscientists & Engineers, pp. 1–5.

Hajiabadi, S.H., Khalifeh, M., van Noort, R., Silva Santos Moreira, P.H., 2023b. Review on geopolymers as wellbore sealants: state of the art optimization for CO2 exposure and perspectives. ACS Omega 8 (26), 23320–23345.

Hamie, H., Hoayek, A., El-Ghoul, B., Khalifeh, M., 2022. Application of non-parametric statistical methods to predict pumpability of geopolymers for well cementing. J. Petrol. Sci. Eng. 212, 110333.

Hansbo, S., 1994. Foundation Engineering. Newnes.

Hardjito, D., Wallah, S.E., Sumajouw, D.M., Rangan, B.V., 2004. On the development of fly ash-based geopolymer concrete. Materials Journal 101 (6), 467–472.

Ismail, A.A., van de Voort, F.R., Sedman, J., 1997. Chapter 4 Fourier transform infrared spectroscopy: principles and applications. In: Paré, J.R.J., Bélanger, J.M.R. (Eds.), Techniques and Instrumentation in Analytical Chemistry. Elsevier, pp. 93–139.

Kamali, M., Khalifeh, M., Eid, E., Saasen, A., 2021a. Experimental study of hydraulic sealability and shear bond strength of cementitious barrier materials. J. Energy Resour. Technol. 144 (2), 023007.

Kamali, M., Khalifeh, M., Eid, E., Saasen, A., 2022a. Experimental study of hydraulic sealability and shear bond strength of cementitious barrier materials. J. Energy Resour. Technol. 144 (2).

Kamali, M., Khalifeh, M., Saasen, A., Delabroy, L., Godøy, R., 2022b. Materials for well integrity–rheological behavior study. In: SPE Norway Subsurface Conference. OnePetro.

Kamali, M., Khalifeh, M., Saasen, A., Godøy, R., Delabroy, L., 2021b. Alternative setting materials for primary cementing and zonal isolation–Laboratory evaluation of rheological and mechanical properties. J. Petrol. Sci. Eng. 201, 108455.

Khale, D., Chaudhary, R., 2007. Mechanism of geopolymerization and factors influencing its development: a review. J. Mater. Sci. 42 (3), 729–746.

Khalifeh, M., 2016. Materials for Optimized P&A Performance: Potential Utilization of Geopolymers.

Khalifeh, M., Hodne, H., Korsnes, R.I., Saasen, A., 2015. Cap rock restoration in plug and abandonment operations; possible utilization of rock-based geopolymers for permanent zonal isolation and well plugging. In: International Petroleum Technology Conference. OnePetro.

Khalifeh, M., Hodne, H., Saasen, A., Integrity, O., Eduok, E.I., 2016a. Usability of geopolymers for oil well cementing applications: reaction mechanisms. In: Pumpability, and Properties, SPE Asia Pacific Oil & Gas Conference and Exhibition. OnePetro.

Khalifeh, M., Motra, H.B., Saasen, A., Hodne, H., 2018a. Potential utilization for a rock-based geopolymer in oil well cementing. In: International Conference on Offshore Mechanics and Arctic Engineering. American Society of Mechanical Engineers, V008T11A037.

Khalifeh, M., Motra, H.B., Saasen, A., Hodne, H., 2018b. Potential utilization for a rock-based geopolymer in oil well cementing. In: ASME 2018 37th International Conference on Ocean, Offshore and Arctic Engineering. American Society of Mechanical Engineers Digital Collection.

Khalifeh, M., Saasen, A., 2020. Introduction to Permanent Plug and Abandonment of Wells. Springer Nature.

Khalifeh, M., Saasen, A., Hodne, H., Godøy, R., Vrålstad, T., 2018c. Geopolymers as an alternative for oil well cementing applications: a review of advantages and concerns. J. Energy Resour. Technol. 140 (9).

Khalifeh, M., Saasen, A., Hodne, H., Motra, H.B., 2019. Laboratory evaluation of rock-based geopolymers for zonal isolation and permanent P&A applications. J. Petrol. Sci. Eng. 175, 352–362.

Khalifeh, M., Saasen, A., Larsen, H.B., Hodne, H., 2017a. Development and characterization of norite-based cementitious binder from an ilmenite mine waste stream. Adv. Mater. Sci. Eng. 2017, 1–7.

Khalifeh, M., Saasen, A., Vrålstad, T., Larsen, H.B., Hodne, H., 2016b. Experimental study on the synthesis and characterization of aplite rock-based geopolymers. J. Sustain. Cement-Based Mater. 5 (4), 233–246.

Khalifeh, M., Todorovic, J., Vrålstad, T., Saasen, A., Hodne, H., 2017b. Long-term durability of rock-based geopolymers aged at downhole conditions for oil well cementing operations. J. Sustain. Cement-Based Mater. 6 (4), 217–230.

Khalili, P., Khalifeh, M., Saasen, A., Naccache, M., 2023. Rheological compatibility of a hardening spacer fluid and oil-based drilling fluid. SPE J. 1–16.

Khater, H.M., 2013. Effect of silica fume on the characterization of the geopolymer materials. Int. J. Adv. Struct. Eng. 5 (1), 1–10.

Kiran, R., et al., 2017. Identification and evaluation of well integrity and causes of failure of well integrity barriers (A review). J. Nat. Gas Sci. Eng. 45, 511–526.

Klein, C., Philpotts, A.R., 2013. Earth Materials: Introduction to Mineralogy and Petrology. Cambridge University Press.

Kumar, S., Mucsi, G., Kristály, F., Pekker, P., 2017. Mechanical activation of fly ash and its influence on micro and nano-structural behaviour of resulting geopolymers. Adv. Powder Technol. 28 (3), 805–813.

Longhi, M.A., Zhang, Z., Rodríguez, E.D., Kirchheim, A.P., Wang, H., 2019. Efflorescence of alkali-activated cements (geopolymers) and the impacts on material structures: a critical analysis. Front. Mater. 6, 89.

Lutgens, F.K., Tarbuck, E.J., Tasa, D., 2014. Essentials of Geology. Pearson, New York.

Mani, S., Pradhan, B., 2020. Investigation on effect of fly ash content on strength and microstructure of geopolymer concrete in chloride-rich environment. In: Materials Today: Proceedings, vol. 32, pp. 865–870.

Marshak, S., 2004. Essentials of Geology. WW Norton.

Muraleedharan, M., Nadir, Y., 2021. Factors affecting the mechanical properties and microstructure of geopolymers from red mud and granite waste powder: a review. Ceram. Int. 47 (10), 13257–13279.

Nadeem, M., et al., 2021. Improved water retention and positive behavior of silica based geopolymer utilizing granite powder. Silicon 1–13.

Nasvi, M., Ranjith, P., Sanjayan, J., Bui, H., 2014a. Effect of temperature on permeability of geopolymer: a primary well sealant for carbon capture and storage wells. Fuel 117, 354–363.

Nasvi, M., Rathnaweera, T., Padmanabhan, E., 2016. Geopolymer as well cement and its mechanical integrity under deep down-hole stress conditions: application for carbon capture and storage wells. Geomech. Geophys. Geo-Energy Geo-Res. 2 (4), 245–256.

Nasvi, M.C.M., Ranjith, P.G., Sanjayan, J., 2013. The permeability of geopolymer at down-hole stress conditions: application for carbon dioxide sequestration wells. Appl. Energy 102, 1391–1398.

Nasvi, M.C.M., Ranjith, P.G., Sanjayan, J., 2014b. Effect of different mix compositions on apparent carbon dioxide (CO2) permeability of geopolymer: suitability as well cement for CO2 sequestration wells. Appl. Energy 114, 939–948.

Nasvi, M.C.M., Ranjith, P.G., Sanjayan, J., Haque, A., Li, X., 2014c. Mechanical behaviour of wellbore materials saturated in brine water with different salinity levels. Energy 66, 239–249.

Nath, P., Sarker, P.K., 2014. Effect of GGBFS on setting, workability and early strength properties of fly ash geopolymer concrete cured in ambient condition. Construct. Build. Mater. 66, 163–171.

Nath, S., Kumar, S., 2013. Influence of iron making slags on strength and microstructure of fly ash geopolymer. Construct. Build. Mater. 38, 924–930.

Nath, S.K., Maitra, S., Mukherjee, S., Kumar, S., 2016. Microstructural and morphological evolution of fly ash based geopolymers. Construct. Build. Mater. 111, 758–765.

Nedunuri, A.S.S.S., Muhammad, S., 2022. The role of zinc sulphate as a retarder for alkali activated binders and its influence on the rheological, setting and mechanical behaviour. Construct. Build. Mater. 344, 128128.

Nematollahi, B., Sanjayan, J., 2014. Effect of different superplasticizers and activator combinations on workability and strength of fly ash based geopolymer. Mater. Des. 57, 667–672.

Nuaklong, P., et al., 2021. Pre-and post-fire mechanical performances of high calcium fly ash geopolymer concrete containing granite waste. J. Build. Eng. 44, 103265.

Ogienagbon, A., Khalifeh, M., 2022. Experimental evaluation of the effect of temperature on the mechanical properties of setting materials for well integrity. SPE J. 1–13.

Okrusch, M., Frimmel, H.E., 2020. Mineralogy: an Introduction to Minerals, Rocks, and Mineral Deposits. Springer Nature.

Omran, M., Hjelm, S., Khalifeh, M., Salehi, S., 2023. Synthesis of sustainable one-part geopolymers for well cementing applications. Geoenergy Sci. Eng. 227, 211822.

Omran, M., Khalifeh, M., Saasen, A., 2022. Influence of activators and admixtures on rheology of geopolymer slurries for well cementing applications. In: SPE Asia Pacific Oil and Gas Conference and Exhibition. SPE, D031S012R003.

Pacheco-Torgal, F., Labrincha, J., Leonelli, C., Palomo, A., Chindaprasit, P., 2014. Handbook of Alkali-Activated Cements, Mortars and Concretes. Elsevier.

Provis, J.L., Van Deventer, J.S.J., 2009. Geopolymers: Structures, Processing, Properties and Industrial Applications. Elsevier.

Prusty, J.K., Pradhan, B., 2020. Effect of GGBS and chloride on compressive strength and corrosion performance of steel in fly ash-GGBS based geopolymer concrete. Mater. Today: Proc. 32, 850–855.

Ramujee, K., PothaRaju, M., 2017. Mechanical properties of geopolymer concrete composites. Mater. Today: Proc. 4 (2), 2937–2945. Part A).

Rong, X., Wang, Z., Xing, X., Zhao, L., 2021. Review on the adhesion of geopolymer coatings. ACS Omega 6 (8), 5108–5112.

Roper, D.S., Kutyla, G.P., Kriven, W.M., 2016. Properties of granite powder reinforced potassium geopolymer. In: Developments in Strategic Ceramic Materials: A Collection of Papers Presented at the 39th International Conference on Advanced Ceramics and Composites, January 25-30, 2015, Daytona Beach, vol. 36. John Wiley & Sons, Florida, p. 3, 8.

Rp, A., 2013. Recommended practice for testing well cements. API RECOMMENDED PRACTICE 10B-2.

Salehi, S., Khattak, J., Saleh, F.K., Igbojekwe, S., 2019. Investigation of mix design and properties of geopolymers for application as wellbore cement. J. Petrol. Sci. Eng. 178, 133–139.

Shah, S.F.A., Chen, B., Oderji, S.Y., Haque, M.A., Ahmad, M.R., 2020. Improvement of early strength of fly ash-slag based one-part alkali activated mortar. Construct. Build. Mater. 246, 118533.

Si, X., Gong, F., Li, X., Wang, S., Luo, S., 2019. Dynamic Mohr–Coulomb and Hoek–Brown strength criteria of sandstone at high strain rates. Int. J. Rock Mech. Min. Sci. 115, 48–59.

Singh, N.B., Middendorf, B., 2020. Geopolymers as an alternative to Portland cement: an overview. Construct. Build. Mater. 237, 117455.

Smith, B.C., 2011. Fundamentals of Fourier Transform Infrared Spectroscopy. CRC press.

Somna, K., Jaturapitakkul, C., Kajitvichyanukul, P., Chindaprasirt, P., 2011. NaOH-activated ground fly ash geopolymer cured at ambient temperature. Fuel 90 (6), 2118–2124.

Tchadjié, L., et al., 2016. Potential of using granite waste as raw material for geopolymer synthesis. Ceram. Int. 42 (2), 3046–3055.

Vafaei, M., Allahverdi, A., 2017. High strength geopolymer binder based on waste-glass powder. Adv. Powder Technol. 28 (1), 215–222.

Vansant, E.F., Van Der Voort, P., Vrancken, K.C., 1995. Characterization and Chemical Modification of the Silica Surface. Elsevier.

Vrålstad, T., et al., 2019. Plug & abandonment of offshore wells: ensuring long-term well integrity and cost-efficiency. J. Petrol. Sci. Eng. 173, 478–491.

Wang, L., et al., 2020. The role of zinc in metakaolin-based geopolymers. Cement Concr. Res. 136, 106194.

Xiao, R., et al., 2020. Strength, microstructure, efflorescence behavior and environmental impacts of waste glass geopolymers cured at ambient temperature. J. Clean. Prod. 252, 119610.

Xue, X., et al., 2018. Inhibiting efflorescence formation on fly ash–based geopolymer via silane surface modification. Cement Concr. Compos. 94, 43–52.

Yao, Z., et al., 2015. A comprehensive review on the applications of coal fly ash. Earth Sci. Rev. 141, 105–121.

Yaseri, S., Hajiaghaei, G., Mohammadi, F., Mahdikhani, M., Farokhzad, R., 2017. The role of synthesis parameters on the workability, setting and strength properties of binary binder based geopolymer paste. Construct. Build. Mater. 157, 534–545.

Yong-Sing, N., et al., 2022. Thin fly ash/ladle furnace slag geopolymer: effect of elevated temperature exposure on flexural properties and morphological characteristics. Ceram. Int. 48 (12), 16562–16575.

Yousefi Oderji, S., Chen, B., Ahmad, M.R., Shah, S.F.A., 2019. Fresh and hardened properties of one-part fly ash-based geopolymer binders cured at room temperature: effect of slag and alkali activators. J. Clean. Prod. 225, 1–10.

Zhang, L., Ahmari, S., Zhang, J., 2011. Synthesis and characterization of fly ash modified mine tailings-based geopolymers. Construct. Build. Mater. 25 (9), 3773–3781.

Zhang, Z., Wang, H., Provis, J.L., Reid, A., 2013. Efflorescence: a critical challenge for geopolymer applications?. In: Concrete Institute of Australia's Biennial National Conference 2013. Concrete Institute of Australia, pp. 1–10.